

# Quality analysis of *in vivo* near-infrared fluorescence and conventional gamma images acquired using a dual-labeled tumor-targeting probe

Jessica P. Houston\*

Texas A&M University  
Photon Migration Laboratory  
College Station, Texas 77842-3012

Shi Ke\*

Wei Wang  
Chun Li

University of Texas M.D. Anderson Cancer Center  
Department of Experimental Diagnostic Imaging  
Box 59, Houston, Texas 77030

Eva M. Sevick-Muraca\*

Texas A&M University  
Photon Migration Laboratory  
College Station, Texas 77842-3012

**Abstract.** The cyclic peptide, cyclopentapeptide cyclo(Lys-Arg-Gly-Asp-phe) (c(KRGDf)), which is known to target  $\alpha v \beta 3$  integrin, is dual-labeled with a radiotracer,  $^{111}\text{In}$ , for gamma scintigraphy as well as with a near-infrared dye, IRDye800, for continuous-wave (cw) imaging of  $\alpha v \beta 3$  positive human M21 melanoma in xenografts. Twenty-four hours after administration of the dual-labeled peptide at a dose equivalent to  $90 \mu\text{Ci}$  of  $^{111}\text{In}$  and 5 nmol of near-infrared (NIR) dye, whole-body gamma scintigraphy and cw imaging was conducted. Image acquisition time was 15 min for the gamma scintigraphy images and 800 ms for the optical images acquired using an NIR sensitive intensified charge-coupled device. The results show that while the target-to-background ratio (TBR) of nuclear and optical imaging were similar for surface regions of interest and consistent with the origin of gamma and NIR radiation from a common targeted peptide, the signal-to-noise ratio (SNR) was significantly higher for optical than nuclear imaging. Furthermore, an analysis of SNR versus contrast showed greater sensitivity of optical over nuclear imaging for the subcutaneous tumor targets. While tomographic reconstructions are necessary to probe TBR, SNR, and contrast for interior tissues, this work demonstrates for the first time the direct comparison of molecular optical and planar nuclear imaging for surface and subsurface cancers. © 2005 Society of Photo-Optical Instrumentation Engineers. [DOI: 10.1117/1.2114748]

Keywords: fluorescence-enhanced optical imaging; continuous wave; photon migration; contrast agent; molecular imaging of cancer.

Paper 04230RR received Nov. 27, 2004; revised manuscript received May 19, 2005; accepted for publication May 25, 2005; published online Oct. 31, 2005.

## 1 Introduction

Nuclear imaging is currently the most effective available medical imaging modality for measuring tracer uptake associated with disease markers as well as with tissue metabolism. Nuclear medicine is prominent in cancer diagnosis, treatment, and prognosis and generally involves the injection of a radionuclide that is targeted for disease specificity. Typically, gamma ray emitting radionuclides are chelated to moieties that are biocompatible, interact with disease markers, or have affinity towards tumor sites.<sup>1-10</sup> Gamma emission can be collected by a gamma camera, producing a scintigram, or a planar projection image that depicts the location of the radionuclide. In addition to planar projection images, tomographically reconstructed images are possible with single photon emission computed tomography (SPECT) and positron emission tomography (PET).

The nuclear tomographic technique of SPECT is based on detecting individual gamma rays emitted at random from the radionuclide, and the tomographic technique of PET is based

upon positron emitters, which interact with the electron rich environment subsequently annihilating to produce two high-energy photons that travel in the opposite direction away from the position of their generation. Their colinear emission enables back-projection to form an image of the radionuclide location. These tomographic imaging approaches may provide millimeter resolution and are limited by the need for ionizing radiopharmaceuticals with finite half-lives and long camera integration times.

Near-infrared (NIR) fluorescence-enhanced optical imaging is similar to nuclear imaging in that a disease targeting molecule conjugated to a radiation-emitting (albeit *non-ionizing radiation*) agent is injected into the body for localization to the diseased site. Upon activation with excitation light, the agent emits fluorescent photons which are then detected externally by sensitive photon detectors. In contrast to nuclear agents, fluorescent agents do not become inactive signal generators after emission but instead are available for repeated activation and relaxation. Excitation and emission in the NIR range are required for imaging tissue, as these energies have low absorption in blood, melanin, and water en-

\*These authors are now located at the Division of Molecular Imaging, Department of Radiology, Baylor College of Medicine, Houston, Texas 77030-3411.

abling penetration in tissues. In contrast to nuclear imaging, high photon count rates enable increased temporal resolution for dynamic imaging.<sup>11</sup> Optical imaging may become a significant molecular imaging tool since it provides digital photo-quality images with low noise and high photon signal emission that can be quantized for pharmacokinetic information<sup>11,12</sup> as well as tomography.<sup>13,14</sup>

Optical imaging in tissues using fluorescence can be employed via several strategies. The imaging strategies generally encompass: (i) detection of endogenous fluorescence; (ii) detection of exogenous fluorescence that is targeted to disease via antibody, polymer, peptide, recombinant protein, or other biocompatible conjugates, or otherwise nontargeted; and (iii) detection of light emitted from quantum dots or other inorganic particles. Detection of bioluminescence represents an optical imaging technique, although not an excitation-emission process. The measurement of fluorescent light emitted from the tissue surface by these strategies may be possible with sensitive image intensifiers coupled to charge-coupled device cameras to provide planar images over the whole body of small animals. Optical imaging by intensified charge-coupled device (ICCD) systems is comparable to conventional nuclear scintigraphy. As ICCDs collect fluorescent photons for image generation, gamma cameras detect gamma emissions and render images that are processed postacquisition to identify diseased tissue sites. Herein we directly compare optical and nuclear imaging using a dual labeled, targeting fluorescence and nuclear agent.

There are presently few examples reported in the literature involving the combination of nuclear and optical imaging. Most studies with small animals have involved reporter gene constructs that either express (i) a visible or red fluorescent protein for excitation and emission (fluorescence); (ii) Renilla or firefly luciferase, which produces visible light in the presence of its exogenous substrate, coelenterazine or D-luciferin (bioluminescence); and/or (iii) express the wild type or mutant herpes simplex virus type 1 thymidine kinase (genotype: HSV1-tk and HSV1-sr39tk, respectively), which phosphorylates PET labeled substrates such as FIAU (2'-fluoro-2'-deoxy-1- $\beta$ -arabinofluranosyl-5-iodouracil], FHBG (9-(4-[<sup>18</sup>F]fluoro-3-hydroxymethylbutyl)guanine), and FPCV(8-[<sup>18</sup>F]fluoropenciclovir).<sup>15-19</sup> These nuclear-optical reporter genes may permit enhanced specificity of the disease with a selectively activated upstream promoter. Unfortunately, the near-term clinical application of gene reporter systems is limited by the need for stable gene transfection and transformation in patients. In this work, we seek to directly compare optical and nuclear imaging using a single targeting moiety containing both a fluorophore and a radionuclide that is exogenously introduced in trace diagnostic concentrations. In previous work, Frangioni and coworkers compared optical and nuclear imaging modalities by evaluating osteoblastic activity in a male nude mouse using a targeting nuclear probe and a second targeting optical probe in order to provide complementary optical and nuclear images for comparison.<sup>20</sup> While other investigators<sup>4</sup> have employed nuclear and optical probe combinations, to date there have been no studies that employ a single, dual-labeled exogenous agent for direct comparison of optical and nuclear imaging modalities. Herein, we use a single probe, dual labeled to provide direct comparison of

optical and nuclear molecular imaging techniques using established figures of merit.

We present a dual-labeled <sup>111</sup>indium (<sup>111</sup>In) and NIR dye, IRDye800, on the cyclopentapeptide cyclo(lys-Arg-Gly-Asp-phe), (c(KRGDf)), which is known to target  $\alpha v \beta 3$  integrin expressed in human melanoma.<sup>21</sup> The use of this probe enables us to image the interaction between a tumor receptor and a targeting ligand in a mouse model by both conventional nuclear imaging and fluorescence-enhanced optical imaging techniques. Since the melanoma is located subcutaneously on the animal, diffusion-based tomography is not valid over the small volumes and short length scales.<sup>22</sup> Furthermore, since direct comparison of fluorescent intensity to gamma ray signals is desired, we conduct the optical imaging using simple, continuous-wave (cw) measurements. The acquired nuclear scintigraphy and cw optical images enable an analysis on the differences between optical and nuclear image qualities.

## 2 Materials and Methods

Fluorescence enhanced optical imaging with an ICCD camera and planar gamma imaging with a small animal gamma camera were performed on a total of six nude mice bearing human melanoma tumors.

### 2.1 Dual-labeled Contrast Agent

For the dual-labeled contrast agent, a peptide containing the amino acid sequence arginine-glycine-aspartic acid, which is known to bind to  $\alpha v \beta 3$  integrin,<sup>23,24</sup> was used. Specifically, Lys-c(KRGDf) was synthesized on linker-PL-DMA resin using Fmoc solid phase chemistry as previously described.<sup>21,25</sup> The radiometal chelator, P-succinamidobenzyl diethylenetriaminepenta-acetic acid, (DTPA) derivative, was first reacted with the  $\alpha$ -amino group of the Lys unit in Lys-c(KRGDf). Subsequently IRDye800 was conjugated to the  $\omega$ -amino group of the Lys unit in DTPA-Lys-c(KRGDf) to give DTPA-Lys(IRDye800)-c(KRGDf). Lastly, the DTPA-Lys(IRDye800)-c(KRGDf) was mixed with <sup>111</sup>InCl<sub>3</sub> to form the final product, <sup>111</sup>In-DTPA-Lys(IRDye800)-c(KRGDf). The NIR dye (IRDye800) excitation/emission wavelengths were measured at 785/830 nm.

### 2.2 Animal Studies

For animal preparation, four- to six-week-old female athymic nude mice (nu/nu 13-21 g) were purchased from Harlan Sprague Dawley, Inc. (Indianapolis, IN). Well-characterized human melanoma tumor cells positively expressing the  $\alpha v \beta 3$  integrin receptors (M21) and human melanoma tumor cells not expressing the  $\alpha v \beta 3$  integrin receptors (M21-L) were maintained at 37 °C in a humidified atmosphere containing 5% CO<sub>2</sub> in Dulbecco's modified Eagle's medium with F12 nutrient and 10% fetal bovine serum. Cells from the positive and negative integrin lines were implanted subcutaneously into the right and left hind region of the six nude mice, respectively. The M21 and M21-L tumor cell lines were kindly provided by Dr. Cheresch (The Scripps Research Institute, La Jolla, CA). The  $\alpha v \beta 3$  integrin positive and integrin negative melanoma cell lines have been used in several studies to in-

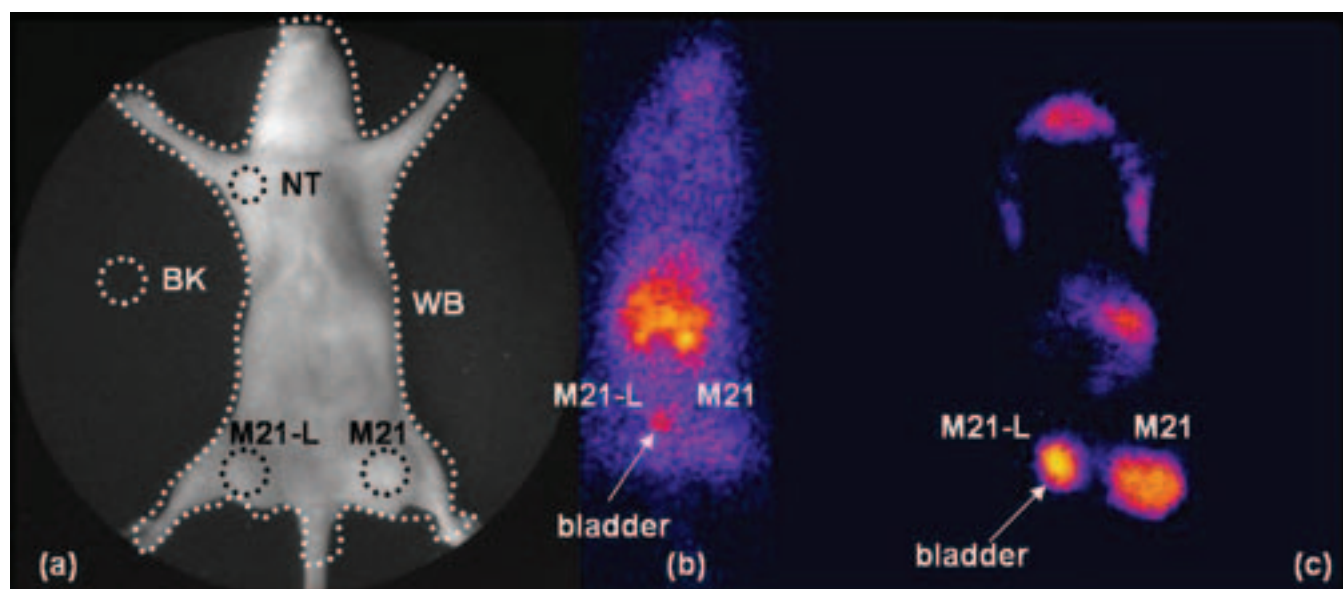


**Fig. 1** White light (a), nuclear scintigram (b), and fluorescence-enhanced optical image (c) of a typical nude mouse xenograph bearing an integrin-positive (M21) tumor in the left thigh (right side: anterior view is displayed by figure) and an integrin-negative (M21-L) tumor in the right thigh (left side: anterior view is displayed by figure). The digital photo of the animal depicts the ROIs selected for the collection of intensity signals either in the positive tumor, negative tumor, or normal tissue regions. The nuclear and optical images show a low signal in the negative (M21-L) tumor (left side), a high signal in the bladder indicating wash-out of the dye, and a high signal in the integrin positive (M21) tumor (right side). The optical image was plotted in a pseudo-color format for enhancement of the intensity scale in the tumor and background. The nuclear image was also adjusted with the same color scale for better discrimination between the several levels of gray provided by the 16-bit image. The nuclear image was acquired after 15 min of integration whereas the optical image was acquired for a total exposure time of 800 ms.

investigate integrin expression and activity in cell signaling, angiogenesis, and proliferation.<sup>26–30</sup> Cheresh and Spiro<sup>27</sup> originally explored the M21 variants by looking at receptor affinity to the RGD amino acid sequence. This investigation led to the isolation of the M21-L, or “M21 Lows,” variant via FACS. The M21-L was found to have low reactivity with the monoclonal antibody, LM142, and ultimately determined to have an altered  $\alpha$  chain level. For the study herein, the six mice were injected with the dual-labeled contrast agent when the M21 and M21-L tumor sizes reached approximately 5 mm in diameter. The dual-labeled contrast agent was intravenously injected into the mouse tail vein at an equivalent dose of 5 nmol of IRDye800 and 90  $\mu$ Ci of <sup>111</sup>indium.

Imaging commenced 24 h after administration of the dual-labeled conjugate. Before imaging, the mice were tagged for identification and anesthetized with Nembutal (50 mg/kg body weight). Animals were then imaged individually with the NIR optical imaging system. After optical imaging, the animals were transferred (approximately 15 min later) to the nuclear gamma camera system to acquire planar scintigraphy images. The nuclear imaging system and NIR optical imaging system are described below.

Animals were maintained in a pathogen-free mouse colony in the Department of Veterinary Medicine (The University of Texas M. D. Anderson Cancer Center, Houston, TX). The facility is accredited by the American Association for Laboratory Animal Care and all experiments were performed in accordance with the guidelines of the Institutional Animal Care and Use Committee.

### 2.3 M.CAM Small Animal Gamma Imaging System

Conventional gamma imaging is accomplished in the following manner: (1) gamma rays upon <sup>111</sup>In decay are emitted isotropically from within the animal, (2) the emitted gamma rays are collimated, (3) the collimated gamma rays strike a scintillation crystal where visible photons (scintillation light) are produced, and (4) the photons are then guided towards a photomultiplier tube (PMT), which collects a ray sum of scintillation light used to generate the projection image.

Conventional gamma imaging was performed in this study with an M.CAM small animal gamma camera (Siemens, Hoffman Estates, IL). This gamma camera is controlled by two central processing units for nuclear acquisition and data processing. The M.CAM houses a high-definition digital detector, which is mounted on a stand that can be manually adjusted and rotated over 90 deg. A collimator is fitted over the entire detector plane and can be removed for replacement. The collimator used for this study was a medium energy low penetration (MELP) with a resolution of 4 to 20 mm and sensitivity of 237 cpm/ $\mu$ Ci. A placement template, covering the collimator, defined the area of the scintillation crystal for placement of the animals over the fixed field of view (FOV) of 54.4  $\times$  39.7 cm<sup>2</sup>. Images were acquired at a 237 keV energy window and by integrating the detector over a time interval of 15 min for which a static planar gamma image was acquired.

The M.CAM system produces a total imaging matrix size of 1024  $\times$  1024 pixels, and the image type was read as a 16-

bit multi pixel array providing intensity counts on the order of  $2^{16}$  levels of gray.

#### 2.4 NIR-Fluorescence-enhanced ICCD Imaging System

Continuous-wave optical imaging of fluorescent NIR photons was performed with a previously developed small animal optical imaging system.<sup>11</sup> The system consists of two complementary detectors, a NIR sensitive image intensifier (model FS9910C ITT Night Vision, Roanoke, VA) and a 16-bit dynamic range full frame Photometrics (model CH350, Roper Scientific, Trenton, NJ) CCD camera. The image intensifier captured the fluorescent NIR signal upon emission from the melanoma tumor site via a 28- to 80-mm zoom Nikon lens (Nikon, Japan). The animal's whole body, an equivalent FOV detection diameter of 11.5 cm (or 8.1 cm for three animals), was focused onto the entire 18-mm-diameter intensifier tube. The image intensifier was selected based upon its optimum photocathode photoresponse [ $\mu\text{A}/\text{lumen}$ ] in the NIR. The full-frame CCD camera imaged the 550-nm amplified light signal output at the intensifier's phosphor screen via a 40-mm Nikon lens (Nikon, Japan). Likewise, to optimize the signal obtained by the NIR system, the CCD camera was designed for a favorable 80% quantum efficiency at 550 nm.

Fluorescence imaging was performed first by expanding a 785 nm excitation source over the body. Here, we used a Thorlabs (80 mW 785 nm, model Sanyo DL7140-201, Newton, NJ) laser diode operating at a dc current of 85 mA and lasing at 785 nm, a suitable wavelength for IRDye800 light absorption. The beam was expanded with a plano-convex lens to a desired circumference over the whole body for area illumination. The diode current was kept constant by a driver (Thorlabs, Inc. Newton, NJ, model LDC500) and the temperature was controlled (Thorlabs, Inc. Newton, NJ, model TEC 2000) at 15°C. A holographic optical diffuser was placed before the plano-convex lens to provide a uniform excitation light field.

Optical filters were fixed to the 28- to 80-mm zoom lens to control fluorescence light input. A 785-nm holographic notch band rejection filter (Kaiser Optical Systems Inc., Ann Arbor, MI, model HNPF-785.0-2.0) was placed in front of the Nikon lens to selectively block the excitation wavelength. Additionally, an 830-nm bandpass filter (Image quality, Andover Corp., Salem, NH, model 830.0-2.0) was stacked with the band rejection filter to selectively pass the emission signal ( $\pm 10$  nm). White-light imaging was acquired by the CCD system, with no optical filtering and with a low power lamp.

#### 2.5 Image Processing

Images acquired from the ICCD camera system and the nuclear M.CAM gamma camera were processed on a 2.6-GHz Windows PC using both the gratis imaging software, ImageJ, (National Institutes of Health, Washington, DC), and the Precision Digital Imaging System software, V++ (Digital Optics, Auckland, New Zealand). ImageJ is an image analysis and processing program in Java and supports both the optical and nuclear image file formats. The nuclear imaging file format, namely an Interfile (containing the file types .hdr and .img) was opened with support from an ImageJ Java script, or "plugin" (<http://www.med.harvard.edu/JPNM/ij/plugins/>

*NucMed.html*). V++ is the Roper Scientific CCD camera software interface with programmable modules for ICCD operation. The processed nuclear images were opened and read as unsigned 16-bit intensity matrices. That is, each pixel was represented by a positive floating point integer up to a total of  $2^{16}$  possible levels of gray. Likewise, the optical file formats (.tif files) were imported into ImageJ or V++ for the intensity calculations described below. Similarly, the optical images were of unsigned data type with integer values ranging from 0 to 65,536.

#### 2.6 Image Analysis by Figures of Merit

In order to assess relative performance of optical imaging and conventional gamma imaging, the mean and standard deviation of intensity counts associated with five primary regions of interest (ROI) were computed (see Fig. 1). Of the five ROI evaluated, one region represented the image "target" and the remaining four regions represented the image "background" for various calculations presented herein.

First, the "hot" area selected for the "target" ROI was the positive tumor, M21. The M21 tumor was fixed as the "target" ROI for all calculations throughout this analysis. The second ROI selected encompassed the negative tumor, M21-L, and this region represented one of the "background" ROI in selected computations. The third ROI surrounded nontumor, or normal tissue (NT). The NT ROI encircled an area on the chest region of the mouse body, and similar to the M21-L ROI, the NT ROI represented a "background" in the computations presented herein. Fourthly, the mean and standard deviation of intensity counts were computed for a ROI that delimited the entire mouse body (WB). The last "background" ROI selected was of the true image background (BK), an area located adjacent to the animal in the surrounding background and not over the body.

The same selected regions of interest corresponding to the M21, M21-L, NT, WB, and BK were used for analysis of optical and nuclear images. That is, the true area of each region remained constant between the nuclear and optical images.

The mean intensity, or mean projected signal,  $\bar{P}$ , is defined below where the integers  $m$  and  $n$  represent the pixel values that make up the  $[i \times j]$  image intensity matrix for the respective regions of interest selected:

$$\bar{P} = \frac{\sum_{i=1}^m \sum_{j=1}^n P_{(i,j)}}{mn}. \quad (1)$$

The optical and nuclear images were evaluated by target-to-background (TBR) and signal-to-noise (SNR) ratios. TBR and SNR are image quality figures of merit used to evaluate signal detection and are often reported in medical imaging analyses.<sup>31-35</sup> The TBR and SNR are computed by:

$$TBR = \frac{\bar{P}^t}{\bar{P}^b} \quad (2)$$

**Table 1** Parameters used to collect images using the intensified CCD camera system and the M.CAM small animal gamma imager. All images were obtained under the instrumentation parameters outlined, with the exception of one M.CAM image that was arbitrarily cropped to  $648 \times 900$  pixels (resolution unchanged) and three animals that were imaged with a smaller field of view during the optical imaging study (values in parentheses).

Modality	Integration time (s)	Total pixels		Field of view		True resolution size ( $\mu\text{m}/\text{pixel}$ )
		rows	columns	height (cm)	width (cm)	
MCAM	900	652	896	39.7	54.4	609
CCD	0.800	300	300	11.4 (8.1)	11.4 (8.1)	380 (303)

$$SNR = \frac{\bar{P}^t - \bar{P}^b}{\sqrt{\frac{\sum_{i=1}^m \sum_{j=1}^n [P_{(i,j)}^b - \bar{P}^b]^2}{mn}}} \quad (3)$$

where the superscript  $t$  represents the mean projected target signal and the superscript  $b$  represents the mean projected background signal.

In addition to correlating the variability in emission signals obtained between optical and nuclear modalities, an analysis of image contrast was assessed. The contrast was calculated by the following relationship:

$$C = \frac{\bar{P}^t - \bar{P}^b}{\bar{P}^b} = TBR - 1. \quad (4)$$

Using these figures of merit described above, we compared: (i) the TBR for both nuclear and optical techniques; (ii) the SNR as a function of integrated area for optical and nuclear images; and (iii) the contrast achievable from both the optical and nuclear images.

### 3 Results

Figure 1 shows typical nuclear gamma and fluorescence-enhanced optical images of a nude mouse bearing the M21 and M21-L tumors 24 h postinjection of the dual-labeled contrast agent. Both images are presented on equivalent pseudo-color schemes and were acquired with the imaging specifications listed in Table 1. The optical image resolution was  $380 \mu\text{m}/\text{pixel}$  (or  $303 \mu\text{m}/\text{pixel}$ , for three animals imaged with a slightly decreased field of view) and the nuclear image resolution was  $609 \mu\text{m}/\text{pixel}$ . Notably, the total integration time required for the acquisition of the optical image was 800 ms while the projected gamma scintigram took a total of 15 min to acquire.

Despite an equivalent dynamic range, the conventional scintigram and optical image (see Fig. 1) have obvious differences in appearance. The M21 tumor is clearly delineated in the optical image; the M21 ROI intensity is much higher in contrast to the background M21-L tumor. Note however the elevated intensity in the optical image most apparent in the animal's neck and abdomen region. The signal at those regions can be attributed to elevated fluorescence signals owing to an irregularity in the expanded excitation beam as well as excitation light leakage from the reflected laser light. Alterna-

tively, the nuclear scintigram of the same animal appears noisy and the tumor is hard to delineate. The scintigram displays low contrast between the M21 ROI and the rest of the body. This reduction in contrast, common in nuclear imaging, arises due to the scatter of gamma rays which are captured into the collimator wells and contribute to the high background signal.

In addition, in a few of the images (as can be noted by example of Fig. 1) the uptake of the dual-labeled peptide in the liver and kidneys is evident in the nuclear scan (i.e., the saturated intensity signal in the abdomen region) but not in the optical scan. Owing to the lower energetics and greater attenuation experienced by NIR photons in comparison to gamma emission, cw planar imaging is surface weighted as evidenced by Fig. 1. While tomographic diffusion approaches for 3-D interior imaging have been developed in large tissue volumes<sup>13,14,36</sup> and in small tissue volumes,<sup>37,38</sup> diffusion-based approaches are invalid for small animal imaging and the length scales under consideration in this study. While radiative transport equation (RTE)-based tomography is currently under development for small animal optical imaging<sup>39</sup> for comparison with PET or SPECT, we use currently available nontomographic, cw imaging and gamma scintigraphy to compare optical and nuclear imaging modalities.

Table 2 summarizes six image quality factors computed from the nuclear and optical images: (1) the WB ROI area [ $\text{cm}^2$ ], (2) the M21, M21-L, and NT ROI areas [ $\text{cm}^2$ ], (3) the mean projected signal from the M21 tumor ROI, (4) the mean projected signal from the WB ROI, (5) the mean projected signal from the M21-L tumor ROI, and (6) the mean projected signal from the NT ROI. The mean projected signals were computed from Eq. (1), and the total tumor and whole body areas ranged from 0.8 to  $1.2 \text{ cm}^2$  and 40 to  $45 \text{ cm}^2$ , respectively. Owing to the successful targeting of the dual-labeled probe, the mean intensity in the M21 ROI was higher than the M21-L ROI for both the gamma scintigram and optical image. The average intensity (a.u.) in the M21 ROI for the six optical images was  $1138.4 (\pm 529)$  and  $1257.5 (\pm 507)$ , for the six scintigrams. In comparison, the average intensity in the M21-L ROI for the six optical images was  $701.6 (\pm 330)$  and  $860.9 (\pm 352)$ , for the six scintigrams.

The TBR figures of merit resulting from each imaged animal are summarized in Table 3. The TBR values, computed by Eq. (2), are presented for the three background regions of interest: (1) M21 target to M21-L background, (2) M21 target to NT background, and (3) M21 target to WB background. The average M21 tumor to M21-L tumor ratios for optical

( $1.4 \pm 0.3$ ) and nuclear ( $1.5 \pm 0.2$ ) were similar based on a statistical significance analysis using a paired t-test ( $\alpha = 0.05$ ). The average M21:NT ratios from the acquired optical and nuclear images were  $1.3 (\pm 0.2)$  and  $1.5 (\pm 0.5)$ , and the similar TBR ratios with the whole body as the “background” (M21:WB) for optical and nuclear resulted in  $1.6 (\pm 0.3)$  and  $1.6 (\pm 0.7)$ , respectively.

Table 3 also lists the SNR computed by Eq. (3) from the optical and nuclear image data. The SNR using the M21 and M21-L tumor ROIs was greater from measurements acquired by the ICCD system than from measurements acquired by the M.CAM (statistically significant, P value =  $1.3 \times 10^{-6}$ ). In fact, the maximum SNR value among all six optical images was 7.7 dB. The SNR from the scintigram corresponding to the same optical SNR was 0.3 dB. The average SNR (a.u.) from the optical images was  $4.7 (\pm 0.7)$  and  $0.78 (\pm 0.5)$  from the nuclear images. The SNR and TBR for the six animals are presented by a bar plot in Fig. 2.

The image contrasts computed by Eq. (4) for all six xenografts are listed in Table 3. The contrast was determined by the mean projected signal in the M21 tumor and the mean projected signal in the M21-L tumor. The tumor was detected over the background at an elevated contrast by the M.CAM system with an average contrast of  $0.5 (\pm 0.3)$  as opposed to  $0.4 (\pm 0.2)$ , the average contrast obtained from the ICCD system.

Figure 3 is a plot of the SNR versus contrast for selected contrast values arranged in increasing magnitude and computed from all six mice. The contrast and SNR displayed by Fig. 3 were computed using the M21 tumor and BK ROIs. That is, the true background signal was compared to the highest signal present in the images, the tumor intensity. This analysis permits a comparison between nuclear and optical image noise floor. Because SNR and contrast are proportional, their linearity provides an outlook on the tumor “detectability” for various levels of image contrast.<sup>40</sup> The SNR required to achieve a specified contrast was lower for the nuclear system than for the optical system. The ICCD camera system was estimated to have a 200+ fold greater sensitivity at the lower contrast values than the nuclear M.CAM imager.

## 4 Discussion

To date, optical techniques have yet to demonstrate the robust detection of cancer in humans that nuclear systems can clinically provide. In this work, we identify the features of fluorescence optical imaging that give rise not only to improvements in optical image quality but also to sensitive acquisition of whole body fluorescent signals using a simple ICCD system. Herein, we have shown that surface melanoma tumors can be easily delineated in all six optical images, while the tumor boundary could not be identified (on a qualitative level) by the gamma images using a single, dual-labeled targeting agent. Several factors that contribute to these differences in measured signal are discussed below.

First, although the functional imaging aims of optical and nuclear techniques are similar, it should be prefaced that the purpose of nuclear imaging modalities used in clinical practice is not strictly to define superficial tumor margins. Rather, nuclear systems play dominant roles for bone scans, lymphoscintigraphy, immunoscintigraphy, and the tracing of diseases

(e.g., cancers, Alzheimer’s, Parkinson’s, AIDS dementia, etc.).<sup>41,42</sup> PET and SPECT are employed over conventional gamma imaging and provide improved image quality and sensitivity. In this study we compare conventional gamma imaging to NIR optical imaging for superficially localized tumors in small animals; both are nontomographic methods with instrumentation designed for small animal imaging.

Second, in order to provide an impartial comparison of nuclear and optical signals, a well-documented and equally detectable contrast agent dose must be established. The dual-labeled peptide,  $^{111}\text{In}$ -DTPA-Lys(IRDye800)-c(KRGDf), used in this study was synthesized for a 1:1 molar ratio of DTPA to conjugated IRDye800. After addition of the radiolabel,  $^{111}\text{In}$ , a final product equivalent to  $20 \mu\text{Ci}$  of radioisotope per nmol of fluorophore was obtained. Indeed the specific activity can be altered by varying the amount of  $^{111}\text{In}$  to be chelated to DTPA-Lys(IRDye800)-c(KRGDf). The total specific activity however, should be balanced for adequate detection of both radio and fluorescent signals. When applied to the clinical setting, radionuclide dosimetry is calculated based on realistic integration times (for patient comfort), radiation exposure (for patient safety), half-life and energy of the isotope, and the minimum detectable signal. Typical clinical intravenous injection doses of Octreoscan ( $^{111}\text{In}$ -D-Phe-DTPA-octreotide) change depending on imaging circumstances ( $3 \text{ mCi}$  to  $6.0 \text{ mCi}$ ),<sup>43,44</sup> and as clinical doses vary so do experimental doses in small animals. Despite a  $> 10^3$  lower bodyweight, mice may be administered 100 times lower doses than humans in order to obtain an adequate signal at realistic integration times. It is noteworthy that the tracer dose does not linearly scale with body mass. Our small animal study required  $3.3 \text{ MBq}$   $^{111}\text{In}$  in order to detect ligand receptor interaction. Similar doses ranging from  $1.8 \text{ MBq}$  to  $7.2 \text{ MBq}$  have been used in small animals with  $^{111}\text{In}$ ,  $^{18}\text{F}$ , and  $^{99}\text{Tc}$ , for studies involving targeting of a radiolabel to the  $\alpha v \beta 3$  integrin via an RGD peptide conjugate.<sup>28,29,45</sup>

Despite controlled fluorophore and isotope specific activities, the high fluorescent photon sensitivity of the ICCD system may be due to the theoretically larger number of fluorescent photons available for imaging over the available gamma rays emitted from the animal. Indeed, the number of radiative events per second emitted by a fluorescent dye can be several orders of magnitude greater than the total emitted by a radionuclide of the same quantity. For example,  $^{111}\text{In}$  has a specific activity of  $4.2 * 10^6 [\text{Ci/g}]$ . To quantify this in terms of emitted disintegrations, the rationale is:

$$\begin{aligned} \frac{4.2 * 10^6 \text{Ci}}{\text{g}} \times \frac{3.7 * 10^{10} \text{Bq}}{\text{Ci}} \times \frac{1 \text{ event/sec}}{\text{Bq}} \\ = 1.5 * 10^{19} \text{ event/sec} \cdot \text{g}^{-1}. \end{aligned}$$

A direct comparison of this activity to the fluorescent dye IRDye800, which has a molecular weight of  $1166 \text{ g/mol}$  and a fluorescent lifetime estimated at  $0.5 \text{ ns}$ , produces:

**Table 2** Summary of the mean projected signals for the M21 tumor ROI, the whole body (WB) ROI, the M21-L ROI, and the normal tissue (NT) ROI. All mean intensity values listed in the table were computed following Eq. (1). The resulting ROI data are from the ICCD imaging system and M.CAM system's measured 16-bit intensities (a.u.). The error bar values are standard deviations computed on the mean projected signal.

Animal Number	Image modality	WB ROI area (cm <sup>2</sup> )	WB ROI mean projected signal (a.u.)	M21, M21-L, and NT ROI area (cm <sup>2</sup> )	M21 ROI mean projected signal (a.u.)	M21-L ROI mean projected signal (a.u.)	NT ROI mean projected signal (a.u.)
1	M.CAM	45	705.4 (+/-) 1116.5 814.2	1.2	1352.6 (+/-) 623.2 1539.5	896.4 (+/-) 498.1 924.4	803.4 (+/-) 614 955.0
	ICCD		(+/-) 319.9		(+/-) 294.7	(+/-) 141.5	(+/-) 139.3
2	M.CAM	45	579.2 (+/-) 904.6 762.2	1.2	1267.6 (+/-) 714.5 1290.2	786.6 (+/-) 477.9 883.2	777.7 (+/-) 549.0 893.4
	ICCD		(+/-) 244.1		(+/-) 158.9	(+/-) 84	(+/-) 80.9
3	M.CAM	45	742.3 (+/-) 1164.6 824.8	1.2	1138.3 (+/-) 578.3 1471.7	987.7 (+/-) 547.1 981.2	936.3 (+/-) 682.8 1029.3
	ICCD		(+/-) 288.3		(+/-) 180.3	(+/-) 120.6	(+/-) 107
4	M.CAM	40	924.6 (+/-) 1318.4 660.9	0.82	1117.3 (+/-) 582.6 817.1	684.9 (+/-) 453 691.9	1177.6 (+/-) 788.7 781.3
	ICCD		(+/-) 123.5		(+/-) 77.6	(+/-) 29.3	(+/-) 59.4
5	M.CAM	40	872.6 (+/-) 1312.9 652.6	0.82	1075.2 (+/-) 629.9 789.5	826.0 (+/-) 506.1 710.7	1085.4 (+/-) 749.7 773.1
	ICCD		(+/-) 113.1		(+/-) 90.1	(+/-) 38.7	(+/-) 53.5
6	M.CAM	40	923.8 (+/-) 1302.3 662.8	0.82	1594.0 (+/-) 816.3 922.6	850.0 (+/-) 583.1 713	708.8 (+/-) 529.9 762.6
	ICCD		(+/-) 124.9		(+/-) 889.1	(+/-) 42.4	(+/-) 44.6

$$\frac{1 \text{ mole}}{1166g} \times \frac{6.02 * 10^{23} \text{ molecule}}{\text{mole}} \times \frac{0.5 * 10^9 \text{ event/molecule}}{\text{sec}}$$

$$= 2.6 * 10^{29} \text{ event/sec} \cdot g^{-1}.$$

Thus, an equivalent “specific activity” for the fluorophore and radionuclide in theory provide significantly different amounts of photons emitted per second ( $10^{10}$ ). Owing to this low sensitivity, nuclear scans require several minutes for data collection. Optical techniques may be favorable for the clinic because they require only a fraction of a second to resolve a fluorescent image.

The discrepancy between the theoretical difference in sensitivity and the actual observed image sensitivity can be explained by the comparative attenuation of NIR and gamma rays during tissue propagation. In tissue, gamma rays attenuate to a much lesser extent than NIR photons. For example, with a linear attenuation coefficient of  $\mu=0.16 \text{ cm}^{-1}$  for a gamma ray, and a reduced scattering and absorption coefficient

of  $\mu'_s=10 \text{ cm}^{-1}$  and  $\mu_a=0.1 \text{ cm}^{-1}$  for NIR photons in thick tissue, a rough estimate of the attenuation of gamma and NIR intensity across 5 cm of tissue can be made:

$$I_{\text{gamma}} = I_0 e^{-\mu L} = 1 \cdot e^{-0.16 * 5} = 0.45$$

$$I_{\text{optical}} = I_0 e^{-\mu L} = 1 \cdot e^{-10.1 * 5} = 1 * 10^{-22}$$

showing that almost 50% of gamma rays are transmitted and much less than 0.01% of optical NIR photons are transmitted through an equivalent tissue depth. Attenuation unquestionably depends on the radiation energy; for example  $\mu \cong 0.16 - 0.35 \text{ cm}^{-1}$  for photon energies of 30 to 100 keV and  $\mu_s=100-300 \text{ cm}^{-1}$  for NIR photons, where scattering dominates.<sup>46</sup> Additionally, photons and gamma rays experience different types of scattering (i.e., Rayleigh versus Compton) in soft tissue.

**Table 3** Target-to-background ratios, signal-to-noise ratios, and contrast values computed following Eqs. (2), (3), and (4). The SNR value is from the (M21) target and (M21-L) background. The resulting TBR values for the (i) (M21) target with (M21-L) background, the (ii) (M21) target with (NT) background, and the (iii) (M21) target with (WB) background are outlined. The contrast results were computed using the target (M21) tumor and the background (M21-L) tumor. The error bars are relative standard deviation values propagated for the computed ratios.

Animal Number	Image modality	SNR M21 & M21-L	TBR M21:M21-L	TBR M21:NT	TBR M21:WB	Contrast M21:M21-L
1	MCAM	0.9 (+/-) 1.8	1.5 (+/-) 0.7	1.7 (+/-) 0.9	1.9 (+/-) 2.3	0.51
	CCD	4.3 (+/-) 0.5	1.7 (+/-) 0.3	1.6 (+/-) 0.2	1.9 (+/-) 5.8	0.67
2	MCAM	1.0 (+/-) 1.9	1.6 (+/-) 0.8	1.6 (+/-) 0.9	2.2 (+/-) 1.9	0.61
	CCD	4.8 (+/-) 0.5	1.5 (+/-) 0.2	1.4 (+/-) 0.2	1.7 (+/-) 8.7	0.46
3	MCAM	0.28 (+/-) 5.3	1.2 (+/-) 0.7	1.2 (+/-) 0.9	1.5 (+/-) 2.1	0.02
	CCD	4.1 (+/-) 0.5	1.5 (+/-) 0.2	1.4 (+/-) 0.2	1.8 (+/-) 8.7	0.50
4	MCAM	1.0 (+/-) 1.8	1.6 (+/-) 0.8	1 (+/-) 0.9	1.2 (+/-) 2	0.63
	CCD	4.3 (+/-) 0.7	1.2 (+/-) 0.1	1.1 (+/-) 0.1	1.2 (+/-) 11.8	0.18
5	MCAM	0.5 (+/-) 3.3	1.3 (+/-) 0.9	1 (+/-) 0.9	1.2 (+/-) 1.8	0.30
	CCD	6.0 (+/-) 0.3	1.3 (+/-) 0.1	1.2 (+/-) 0.1	1.4 (+/-) 18.7	0.32
6	MCAM	1.3 (+/-) 1.5	1.9 (+/-) 0.9	2.3 (+/-) 0.9	1.7 (+/-) 2.1	0.88
	CCD	5.3 (+/-) 0.29	1.3 (+/-) 0.1	1.2 (+/-) 0.1	1.4 (+/-) 1.4	0.29

A large part of NIR attenuation for fluorescence-enhanced imaging is due to scattering and absorption as well as the decay kinetics of the fluorophore. Excitation light attenuates before reaching the embedded fluorophore and the quantum efficiency,  $\phi$ , of the fluorophore reduces the amount of fluorescent light that is re-emitted. Upon traveling back to the tissue surface, fluorescent photon attenuation occurs. Ultimately the photon fluence measured at the tissue surface is reduced and for the small animal imaging described herein, its attenuation must be predicted by the full radiative transport equation.

A last and important preface to nuclear and optical imager differences that may impact equal comparison is camera resolution. The CCD chip has fixed, 24- $\mu\text{m}$ -size wells, thus the image resolution, or actual pixel size, may vary depending on the field of view chosen and achieved using any typical camera focusing lens. For the ICCD system, the resolution on an optical image is ultimately limited by the image intensifier; the CCD images a constant FOV at the phosphor screen, which likewise can be controlled by a simple zoom lens. Unlike the optical system however, the M.CAM has a fixed field of view, therefore the resolution is fixed for a given collimator size.

The comparative target to background ratios that are presented reflect some distinguishing qualities between the planar optical and nuclear image display. The M21:M21-L TBR values were analyzed and found to be similar; this similarity was anticipated because the contrast agent was dual-labeled causing the radionuclide and fluorophore to have an equal relative accumulation between the M21 and M21-L tumor.

Yet upon viewing the ROI intensities in the actual optical and nuclear images (Fig. 1) this TBR similarity is less apparent. There is little signal delineating the gamma image M21 ROI over the M21-L ROI, which indicates a high variance in pixel intensity resulting from a raised background signal. The large background signal in the nuclear scintigram reflects the fact that gamma cameras detect scattered gamma rays that are emitted from deep tissue sections. Thus, any annihilated photons that emit from the liver, kidneys, and deeper tissue (>5 mm) are imaged and contribute to the total mean projected signal. Moreover, gamma rays that scatter into a single collimating well and emit from locations not adjacent to that well are weighted the same as those photons that travel in a straight trajectory from the tumor to the collimator. Thus, the deviation in pixel intensity values is much greater for the M.CAM than for the ICCD system.

Additionally, the similarities between the optical and nuclear M21:NT ratios and optical and nuclear M21:WB ratios further demonstrate that the dual-labeled agent was target-specific to the  $\alpha v \beta 3$  integrin positive melanoma tumor. The nuclear and optical detectors equally discriminated between targeted signals and nontargeted signals from the background of the entire animal body and normal tissue regions. Yet, the optical and nuclear imaging systems appear to detect different background signals because (i) optical ICCD sensitivity is weighted toward shallow, subsurface photons; (ii) attenuated optical signals are often reported at suppressed intensities relative to nonattenuated signals owing to excessive excitation light leakage; (iii) conventional gamma camera systems detect gamma rays from any depth or location in the

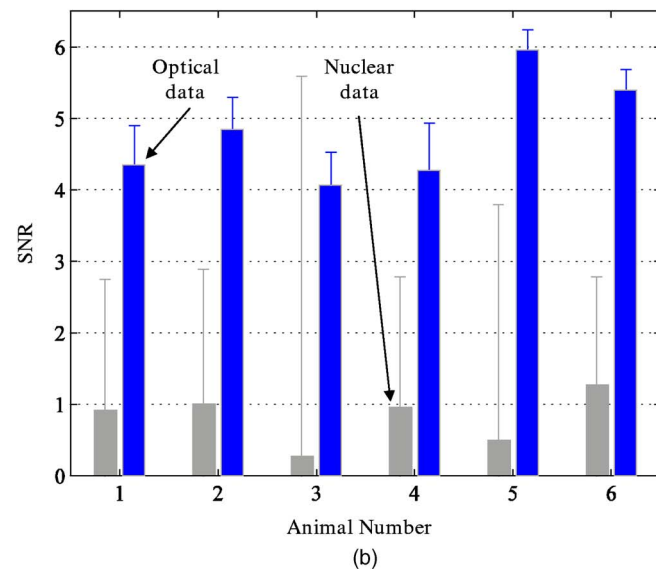
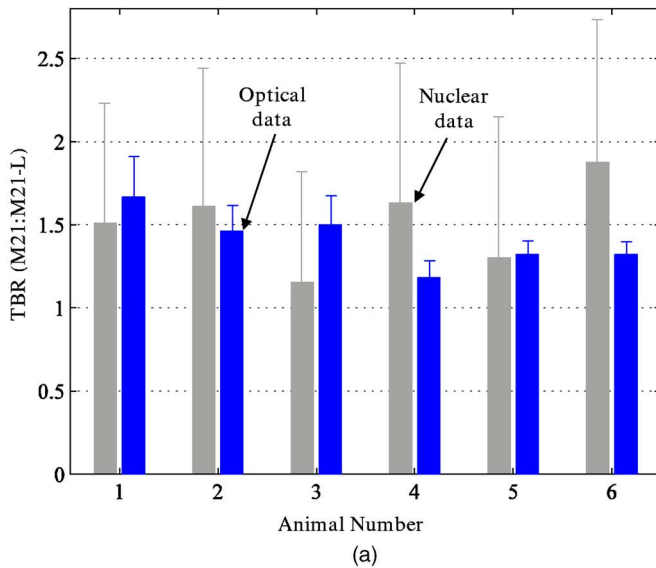


**Fig. 2** The bar plots present (a) target-to-background ratios and (b) signal-to-noise ratios of the M21 tumor region of interest to the M21-L tumor background region of interest computed from NIR (dark-shaded) and gamma (light-shaded) images for all six animals studied. Error bars represent the relative standard deviation. The TBRs predicted from the ICCD and the MCAM yield statistically similar results (paired t-test with  $\alpha=0.05$ ). On the contrary, the SNR values predicted from the ICCD and the MCAM yield statistically different results (paired t-test with P value equal to  $1.3e-6$ ), thus indicating that the ICCD imager produces on the average higher SNR values than does the M.CAM imager.

body with equal sensitivity; and (iv) gamma systems detect photons that travel in a mostly linear fashion through the body with little attenuation. Therefore the background signals from the optical M21:WB and M21:NT ratios are from fluorescence emitted by tissues and blood located a few millimeters below the skin's surface as well as excitation light leakage through the optical filters. Alternatively, the gamma camera TBRs are indicative of the total radio-nuclide emissions from within the whole body relative to the gamma ray emission from the entire tumor volume.

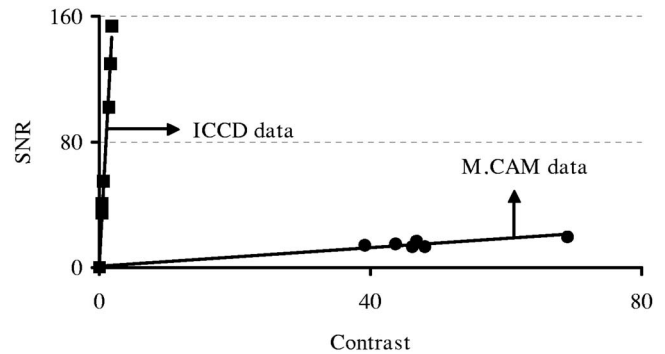


**Fig. 3** SNR versus contrast. SNR was calculated using Eq. (3) and contrast computed from Eq. (4) using optical and nuclear image intensity data (a.u.). The expected linear relationship between the SNR and contrast are different between optical and nuclear. That is, the optical imaging SNR versus contrast slope is dramatically increased over the nuclear imaging SNR versus contrast.

Unlike the TBR ratios, the statistically different SNR may be an indication of the reduced noise floor that an ICCD system provides. ICCDs are typically operated under shot-noise limited conditions,<sup>47</sup> where photon noise is the limiting noise factor. Therefore, when high photon signals emitting from the tumor are detected, the Poisson distributed shot noise becomes relatively much smaller and this is reflected in the image output SNR. The SNR computed from the conventional gamma images is much lower than the optical owing also to the imaging system's intrinsic signal-to-noise characteristics. The radioactive decay and gamma detection variance is closer to the gain, or sensitivity of the detector; this is reflected in the scintigram pixel values. However the favorable SNR of optical over nuclear may dramatically decrease when comparing deeply seated tumors as in the case of human imaging. Consider two targets 0.5 and 2 cm deep to be imaged using planar optical and nuclear imaging. The noise associated with each of the imaging modalities remains constant as the depth of the target increases. Assuming that the gamma emitting targets are of equal energy, the signal from the two centimeter depth ( $e^{-(0.16*2)}=0.7$ ) will be attenuated by a difference of 0.2 in comparison to that emitted from the target 0.5 cm in depth ( $e^{-(0.16*0.5)}=0.9$ ). For optical imaging, greater attenuation occurs with typical tissue scattering and absorption coefficients such as  $\mu'_s=10 \text{ cm}^{-1}$  and  $\mu_a=0.1 \text{ cm}^{-1}$ . Using these optical properties for a total attenuation coefficient of  $\mu_t=10.1$ , the comparative attenuation of photons from 0.5 cm to 2 cm is  $0.006$  and  $2*10^{-9}$ , respectively, a magnitude difference of  $10^6$ . Of course, these calculations do not consider the half-life of the radiotracer, wherein the SNR of fluorescent targets at all depths may be significantly greater than that of a spent tracer at any depth.

Yet for detection of surface signals, plotting the SNR versus contrast further demonstrates improved sensitivity by the ICCD system. A high photon signal detected by the ICCD system yields a large SNR value despite the low contrast between the tumor and background. For the SNR contrast plots, the background value used was a true background ROI; a selected area outside of the animal body was used as the baseline noise signal. The change in optical SNR relative to the change in optical image contrast is more than 200-fold greater

than the conventional gamma camera SNR-contrast gradient. Moreover, fluorescence-enhanced optical imaging has potential for improved SNR with better reduction in the excitation light noise. With the increase in intensified CCD sensitivity, excitation light is hard to eliminate from the total detected signal because of the fraction of excitation light (19%)<sup>48</sup> passed through standard band rejection and optical bandpass filters.

Although this work demarcates favorable optical image quality relative to a conventional gamma camera, multimodality imaging combinations are truly complementary with neither imaging method providing completely autonomous diagnostic information. In this work however, the combined imaging methods provided a comparative tool for optical ICCD camera image quality assessment, which is essential for clinical translation of functional planar NIR imaging. Upon comparison to conventional nuclear imaging, it is evident that optical imaging with ICCD cameras is highly sensitive to photons emanating from superficial depths. Additionally, as optical tomography is developed for multipixel techniques on larger volumes,<sup>49</sup> assessment of the target detection for small target sizes and greater target depths is increasingly important for locating the tumor position through a three-dimensional map in thick (>1 cm) human tissues.

#### Acknowledgments

This work was supported in parts by National Institute of Health Grants, R01 EB003132(EMS) and R01 EB00174(CL).

#### References

1. S. Wang, J. Luo, D. A. Lantrip, D. J. Waters, C. J. Mathias, M. A. Green, P. L. Fuchs, and P. S. Low, "Design and synthesis of [<sup>111</sup>In]DTPA-folate for use as a tumor-targeted radiopharmaceutical," *Bioconjugate Chem.* **8**, 673–679 (1997).
2. S. S. Gambhir, "Molecular imaging of cancer with positron emission tomography," *Nat. Rev. Cancer* **2**, 683–693 (2002).
3. S. S. Gambhir, E. Bauer, M. E. Black, Q. Liang, M. S. Kokoris, J. R. Barrio, M. Iyer, M. Namavari, M. E. Phelps, and H. R. Herschman, "A mutant herpes simplex virus type 1 thymidine kinase reporter gene shows improved sensitivity for imaging reporter gene expression with positron emission tomography," *Proc. Natl. Acad. Sci. U.S.A.* **97**, 2785–2790 (2000).
4. S. Achilefu, A. Srinivasan, M. A. Schmidt, H. N. Jimenez, J. E. Bugaj, and J. L. Erion, "Novel bioactive and stable neurotensin peptide analogues capable of delivering radiopharmaceuticals and molecular beacons to tumors," *J. Med. Chem.* **46**, 3403–3411 (2003).
5. B. A. Siegel, F. Dehdashti, D. G. Mutch, D. A. Podoloff, R. Wendt, G. P. Sutton, R. W. Burt, P. R. Ellis, C. J. Mathias, M. A. Green, and D. M. Gershenson, "Evaluation of <sup>111</sup>In-DTPA-folate as a receptor-targeted diagnostic agent for ovarian cancer: initial clinical results," *J. Nucl. Med.* **44**, 700–707 (2003).
6. B. E. Rogers, H. M. Bigott, D. W. McCarthy, D. Della Manna, J. Kim, T. L. Sharp, and M. J. Welch, "MicroPET imaging of a gastrin-releasing peptide receptor-positive tumor in a mouse model of human prostate cancer using a <sup>64</sup>Cu-labeled bombesin analogue," *Bioconjugate Chem.* **14**, 756–763 (2003).
7. L. Aloj, C. Caraco, M. Panico, A. Zannetti, S. Del Vecchio, D. Teasaro, S. De Luca, C. Arra, C. Pedone, G. Morelli, and M. Salvatore, "In vitro and in vivo evaluation of <sup>111</sup>In-DTPA-Glu-G-CCK8 for cholecystokinin-B receptor imaging," *J. Nucl. Med.* **45**, 485–494 (2004).
8. C. Y. Ke, C. J. Mathias, and M. A. Green, "Folate-receptor-targeted radionuclide imaging agents," *Adv. Drug Delivery Rev.* **56**, 1143–1160 (2004).
9. D. M. Goldenberg, "Perspectives on oncologic imaging with radiolabeled antibodies," *Cancer* **80**, 2431–2435 (1997).
10. C. M. Lahorte, J. L. Vanderheyden, N. Steinmetz, C. Van De Wiele, R. A. Dierckx, and G. Slegers, "Apoptosis-detecting radioligands: current state of the art and future perspectives," *Eur. J. Nucl. Med. Mol. Imaging* **31**, 887–919 (2004).
11. S. Ke, X. Wen, M. Gurfinkel, C. Charnsangavej, Z. Fan, S. Wallace, E. M. Sevick-Muraca, and C. Li, "Near infrared optical imaging of epidermal growth factor receptor in breast cancer xenografts," *Cancer Res.* **63**, 7870–7875 (2003).
12. M. Gurfinkel, A. B. Thompson, W. Ralston, T. L. Troy, A. L. Moore, T. A. Moore, J. D. Gust, D. Tatman, J. S. Reynolds, B. Muggenburg, K. Nikula, R. Pandey, R. H. Mayer, D. J. Hawrysz, and E. M. Sevick-Muraca, "Pharmacokinetics of ICG and HPPH-car for the detection of normal and tumor tissue using fluorescence, near-infrared reflectance imaging: a case study," *Photochem. Photobiol.* **72**, 94–102 (2000).
13. A. Godavarty, M. J. Eppstein, C. Zhang, S. Theru, A. B. Thompson, M. Gurfinkel, and E. M. Sevick-Muraca, "Fluorescence-enhanced optical imaging in large tissue volumes using a gain-modulated ICCD camera," *Phys. Med. Biol.* **48**, 1701–1720 (2003).
14. A. Godavarty, A. B. Thompson, R. Roy, M. Gurfinkel, M. J. Eppstein, C. Zhang, and E. M. Sevick-Muraca, "Diagnostic imaging of breast cancer using fluorescence-enhanced optical tomography: phantom studies," *J. Biomed. Opt.* **9**, 488–496 (2004).
15. R. G. Blasberg, "In vivo molecular-genetic imaging: multi-modality nuclear and optical combinations," *Nucl. Med. Biol.* **30**, 879–888 (2003).
16. J. C. Wu, I. Y. Chen, G. Sundaresan, J. J. Min, A. De, J. H. Qiao, M. C. Fishbein, and S. S. Gambhir, "Molecular imaging of cardiac cell transplantation in living animals using optical bioluminescence and positron emission tomography," *Circulation* **108**, 1302–1305 (2003).
17. P. Ray, A. De, J. J. Min, R. Y. Tsien, and S. S. Gambhir, "Imaging tri-fusion multimodality reporter gene expression in living subjects," *Cancer Res.* **64**, 1323–1330 (2004).
18. A. Jacobs, M. Dubrovin, J. Hewett, M. Sena-Estevés, C. W. Tan, M. Slack, M. Sadelain, X. O. Breakefield, and J. G. Tjuvajev, "Functional coexpression of HSV-1 thymidine kinase and green fluorescent protein: implications for noninvasive imaging of transgene expression," *Neoplasia* **1**, 154–161 (1999).
19. V. Ponomarev, M. Dubrovin, I. Serganova, T. Beresten, J. Vider, A. Shavrin, L. Ageyeva, J. Balatoni, R. Blasberg, and J. G. Tjuvajev, "Cytoplasmically retargeted HSV1-tk/GFP reporter gene mutants for optimization of noninvasive molecular genetic imaging," *Neoplasia* **5**, 245–254 (2003).
20. A. Zaheer, R. E. Lenkinski, A. Mahmood, A. G. Jones, L. C. Cantley, and J. V. Frangioni, "In vivo near-infrared fluorescence imaging of osteoblastic activity," *Nat. Biotechnol.* **19**, 1148–1154 (2001).
21. W. Wang, S. Ke, Q. Wu, C. Charnsangavej, M. Gurfinkel, J. Gelovani, J. L. Abbruzzese, E. M. Sevick-Muraca, and C. Li, "Near-infrared optical imaging of integrin alpha v beta 3 in human tumor xenografts," *Molecular Imaging* **3**, 343–351 (2004).
22. A. D. Kim and A. Ishimaru, "Optical diffusion of continuous-wave, pulsed, and density waves in scattering media and comparisons with radiative transfer," *Appl. Opt.* **37**, 5313–5319 (1998).
23. R. Pasqualini, E. Koivunen, and E. Ruoslahti, "A peptide isolated from phage display libraries is a structural and functional mimic of an RGD-binding site on integrins," *J. Cell Biol.* **130**, 1189–1196 (1995).
24. R. Pasqualini, E. Koivunen, and E. Ruoslahti, "Alpha v integrins as receptors for tumor targeting by circulating ligands," *Nat. Biotechnol.* **15**, 542–546 (1997).
25. C. Li, W. Wang, S. Ke, Q. Wu, J. Houston, E. M. Sevick-Muraca, L. Dong, D. Chow, C. Charnsangavej, and J. P. Gelovani, "Dual optical and nuclear imaging of integrin  $\alpha v \beta 3$  in human melanoma xenografts using a single imaging probe," submitted to *Eur. J. Nucl. Med. Mol. Imaging*.
26. E. Petittler, S. Stromblad, T. L. von Schalscha, F. Mitjans, J. Piulats, A. M. Montgomery, D. A. Cheresch, and P. C. Brooks, "Integrin  $\alpha v \beta 3$  promotes M21 melanoma growth in human skin by regulating tumor cell survival," *Cancer Res.* **59**, 2724–2730 (1999).
27. D. A. Cheresch and R. C. Spiro, "Biosynthetic and functional properties of an Arg-Gly-Asp-directed receptor involved in human melanoma cell attachment to vitronectin, fibrinogen, and von Willebrand factor," *J. Biol. Chem.* **262**, 17703–17711 (1987).
28. R. Haubner, F. Bruchertseifer, M. Bock, H. Kessler, M. Schwaiger, and H. J. Wester, "Synthesis and biological evaluation of a (99m)Tc-labelled cyclic RGD peptide for imaging the  $\alpha v \beta 3$  expression," *Nuklearmedizin* **43**, 26–32 (2004).

29. R. Haubner, H. J. Wester, W. A. Weber, C. Mang, S. I. Ziegler, S. L. Goodman, R. Senekowitsch-Schmidtko, H. Kessler, and M. Schwaiger, "Noninvasive imaging of alpha(v)beta3 integrin expression using 18F-labeled RGD-containing glycopeptide and positron emission tomography," *Cancer Res.* **61**, 1781–1785 (2001).
30. P. C. Brooks, A. M. Montgomery, M. Rosenfeld, R. A. Reisfeld, T. Hu, G. Klier, and D. A. Cheresh, "Integrin alpha v beta 3 antagonists promote tumor regression by inducing apoptosis of angiogenic blood vessels," *Cell* **79**, 1157–1164 (1994).
31. W. T. Philips, "Delivery of gamma-imaging agents by liposomes," *Adv. Drug Delivery Rev.* **37**, 13–32 (1999).
32. H. Palmedo, H. Bender, F. Grunwald, P. Mallmann, P. Zamora, D. Krebs, and H. J. Biersack, "Comparison of fluorine-18 fluorodeoxyglucose positron emission tomography and technetium-99m methoxyisobutylisonitrile scintimammography in the detection of breast tumours," *Eur. J. Nucl. Med.* **24**, 1138–1145 (1997).
33. A. K. Paul, M. Tatsumi, K. Yutani, K. Fujino, K. Hashikawa, and T. Nishimura, "Effects of iterative reconstruction on image contrast and lesion detection in gamma camera coincidence imaging in lung and breast cancers," *Nucl. Med. Commun.* **23**, 103–110 (2002).
34. I. Khalkhali, J. A. Cutrone, I. G. Mena, L. E. Diggles, R. J. Venegas, H. I. Vargas, B. L. Jackson, S. Khalkhali, J. F. Moss, and S. R. Klein, "Scintimammography: the complementary role of Tc-99m sestamibi prone breast imaging for the diagnosis of breast carcinoma," *Radiology* **196**, 421–426 (1995).
35. R. E. Coleman, C. M. Laymon, and T. G. Turkington, "FDG imaging of lung nodules: a phantom study comparing SPECT, camera-based PET, and dedicated PET," *Radiology* **210**, 823–828 (1999).
36. R. Roy, A. B. Thompson, A. Godavarty, and E. M. Sevick-Muraca, "Tomographic fluorescence imaging in tissue phantoms: a novel reconstruction algorithm and imaging geometry," *IEEE Trans. Med. Imaging* **34**, 137–154 (2005).
37. V. Ntziachristos, E. A. Schellenberger, J. Ripoll, D. Yessayan, E. Graves, A. Bogdanov Jr., L. Josephson, and R. Weissleder, "Visualization of antitumor treatment by means of fluorescence molecular tomography with an annexin VCy5.5 conjugate," *Proc. Natl. Acad. Sci. U.S.A.* **101**, 12294–12299 (2004).
38. V. Ntziachristos, C. Bremer, E. Graves, J. Ripoll, and R. Weissleder, "In vivo tomographic imaging of near-infrared fluorescent probes," *Molecular Imaging* **1**, 82–88 (2002).
39. J. C. Rasmussen, A. Joshi, E. M. Sevick-Muraca, J. McGhee, T. Wareing, and G. Failla, "Small animal fluorescence tomography based on the Radiative Transport Equation and time-dependent measurements," Presented at Third Annual Meeting of the Society for Molecular Imaging **4**, 374–375 (2005).
40. J. D. Sain and H. H. Barrett, "Performance evaluation of a modular gamma camera using a detectability index," *J. Nucl. Med.* **44**, 58–66 (2003).
41. F. G. Blankenberg and H. W. Strauss, "Nuclear medicine applications in molecular imaging," *J. Magn. Reson Imaging* **16**, 352–361 (2002).
42. M. G. Pomper and D. A. Hammoud, "Positron emission tomography in molecular imaging. Could the promise of personalized patient care be reaching fruition?," *IEEE Eng. Med. Biol. Mag.* **23**, 28–37 (2004).
43. V. Briganti, M. Matteini, P. Ferri, L. Vaggelli, A. Castagnoli, and C. Pieroni, "Octreoscan SPET evaluation in the diagnosis of pancreas neuroendocrine tumors," *Cancer Biother. Radiopharm.* **16**, 515–524 (2001).
44. M. P. Sandler, R. E. Coleman, J. A. Patton, F. J. T. Wackers, and A. Gotschalk, *Diagnostic Nuclear Medicine*, p. 1272, Lippincott Williams and Wilkins, Philadelphia (2003).
45. M. L. Janssen, W. J. Oyen, I. Dijkgraaf, L. F. Massuger, C. Frielink, D. S. Edwards, M. Rajopadhye, H. Boonstra, F. H. Corstens, and O. C. Boerman, "Tumor targeting with radiolabeled alpha(v)beta(3) integrin binding peptides in a nude mouse model," *Cancer Res.* **62**, 6146–6151 (2002).
46. Z. H. Cho, J. P. Jones, and M. Singh, *Foundations of Medical Imaging*, Wiley, New York (1993).
47. A. B. Thompson and E. M. Sevick-Muraca, "NIR fluorescence contrast enhanced imaging with ICCD homodyne detection: measurement precision and accuracy," *J. Biomed. Opt.* **8**, 111–120 (2002).
48. J. Houston, A. B. Thompson, M. Gurfinkel, and E. M. Sevick-Muraca, "Sensitivity and depth penetration of continuous wave versus frequency-domain photon migration near-infrared fluorescence contrast-enhanced imaging," *Photochem. Photobiol.* **77**, 420–430 (2003); erratum, **78**, 103.
49. A. Godavarty, A. Zhang, M. J. Eppstein, and E. M. Sevick-Muraca, "Fluorescence-enhanced optical imaging of large phantoms using single and simultaneous dual point illumination geometries," *Med. Phys.* **31**, 183–190 (2004).